NANO · MICRO small
www.small-journal.com

Olivine-Type $MgMn_{0.5}Zn_{0.5}SiO_4$ Cathode for Mg-Batteries: Experimental Studies and First Principles Calculations

Carlos Pérez-Vicente, Saúl Rubio, Rafaela Ruiz, Wenhua Zuo, Ziteng Liang, Yong Yang, and Gregorio F. Ortiz**

Magnesium driven reaction in olivine-type $MgMn_{0.5}Zn_{0.5}SiO_4$ structure is subject of study by experimental tests and density functional theory (DFT) calculations. The partial replacement of Mn in Oh sites by other divalent metal such as Zn to get $MgMn_{0.5}Zn_{0.5}SiO_4$ cathode is successfully developed by a simple sol–gel method. Its comparison with the well-known $MgMnSiO_4$ olivine-type structure with $(Mg)_{M1}(Mn)_{M2}SiO_4$ cations distribution serves as the basis of this study to understand the structure, and the magnesium extraction/insertion properties of novel olivine-type $(Mg)_{M1}(Mn_{0.5}Zn_{0.5})_{M2}SiO_4$ composition. This work foresees to extend the study to others divalent elements in olivine-type $(Mg)_{M1}(Mn_{0.5}M_{0.5})_{M2}SiO_4$ structure with M = Fe, Ca, Mg, and Ni by DFT calculations. The obtained results indicate that the energy density can be attuned between 520 and 440 W h kg^{-1} based on two properties of atomic weight and redox chemistry. The presented results commit to open new paths toward development of cathodes materials for Mg batteries.

1. Introduction

The launch of polyanionic $LiFePO_4$ (LFP) type cathode materials by Goodenough's group in 1997,[1] opened a great path for research advancements on Li-ion batteries (LIBs). Nowadays the employment of such materials in commercial batteries has confirmed the great success on the research development of battery technology over the world. Consequently, the research efforts that the scientific community is still pursuing focus on this structural model to unveil enhanced reactions in lithium and magnesium battery fields.[2,3] One of the main limitations of the LFP is the limited capacity for one electron reaction and thus its energy density cannot get over to that of layered oxides. Therefore, alternative silicates with Li_2MSiO_4 (M = Mn, Fe, Co, Ni) stoichiometry are currently studied due to the high theoretical capacity of 333 mA h g^{-1}.[4,5] Additionally, the redox potential should be successfully monitored by the redox (≈manganese) active species. Importantly, the main instabilities caused in the original Mn-tetrahedral environments, structural amorphization during alkali metal extraction and structural distortions should be abated.[5]

This study compares different manganese silicates with Mn in octahedral environment to avoid the instabilities of Mn in tetrahedral sites. Specifically, $MgMnSiO_4$ is used as a model which has an olivine-type structure (similar to LFP) where Mg atoms occupy the so-called M1 site (as Li in LFP) while Mn atoms occupy the M2 site (Fe in LFP) (**Scheme 1**). The chemical formulation is thus $(Mg)_{M1}(Mn)_{M2}SiO_4$.[6,7] Additionally, the comprehensive exchange of Mg and Mn in their respective sites gives the following cation distribution: $(Mg_{1-y}Mn_y)_{M1}(Mg_yMn_{1-y})_{M2}SiO_4$, being the degree of exchange dependent on the sample thermal history.[8,9]

This work aims to determine the structure and Mg extraction/insertion properties from/into $(Mg)_{M1}(Mn_{0.5}Zn_{0.5})_{M2}SiO_4$. The replacement of half amount of Mn atoms in the octahedral sites by other divalent elements such as Zn^{2+} could have an impact on the voltage and the energy density as foreseen by DFT calculations. The calculated voltage during Mg reaction for $MgMnSiO_4$ is ≈2.9 V, while the higher voltage of ≈3.2 V is obtained in the case of $(Mg)_{M1}(Mn_{0.5}M_{0.5})_{M2}SiO_4$ (M = Ca and Ni). However, the higher atomic weight of Ni penalizes its energy density, as compared with lighter elements such as M = Ca or Mg. The $(Mg)_{M1}(Mn_{0.5}Zn_{0.5})_{M2}SiO_4$ cathode achieves experimentally 120 mA h g^{-1} with an average voltage of ≈2 V.

2. Results and Discussion

2.1. Structure and Mg Extraction: Case of $MgMnSiO_4$

The calculated unit cell parameters (a = 10.460(5) Å, b = 6.134(3) Å, c = 4.817(2) Å, and V = 309.0(2) $Å^3$) from the refined X-ray diffraction (XRD) pattern are in good agreement with previous

C. Pérez-Vicente, S. Rubio, R. Ruiz, G. F. Ortiz
Department of Inorganic Chemistry and Chemical Engineering
University Research Institute for Energy and the Environment (IQUEMA)
University of Córdoba
Campus of Rabanales, Marie Curie Building E-14071 Córdoba, Spain
E-mail: q72maorg@uco.es
W. Zuo, Z. Liang, Y. Yang, G. F. Ortiz
State Key Laboratory for Physical Chemistry of Solid Surfaces
Department of Chemistry
College of Chemistry and Chemical Engineering
Xiamen University
Xiamen 361005, P. R. China
E-mail: yyang@xmu.edu.cn
The ORCID identification number(s) for the author(s) of this article can be found under https://doi.org/10.1002/smll.202206010.

DOI: 10.1002/smll.202206010

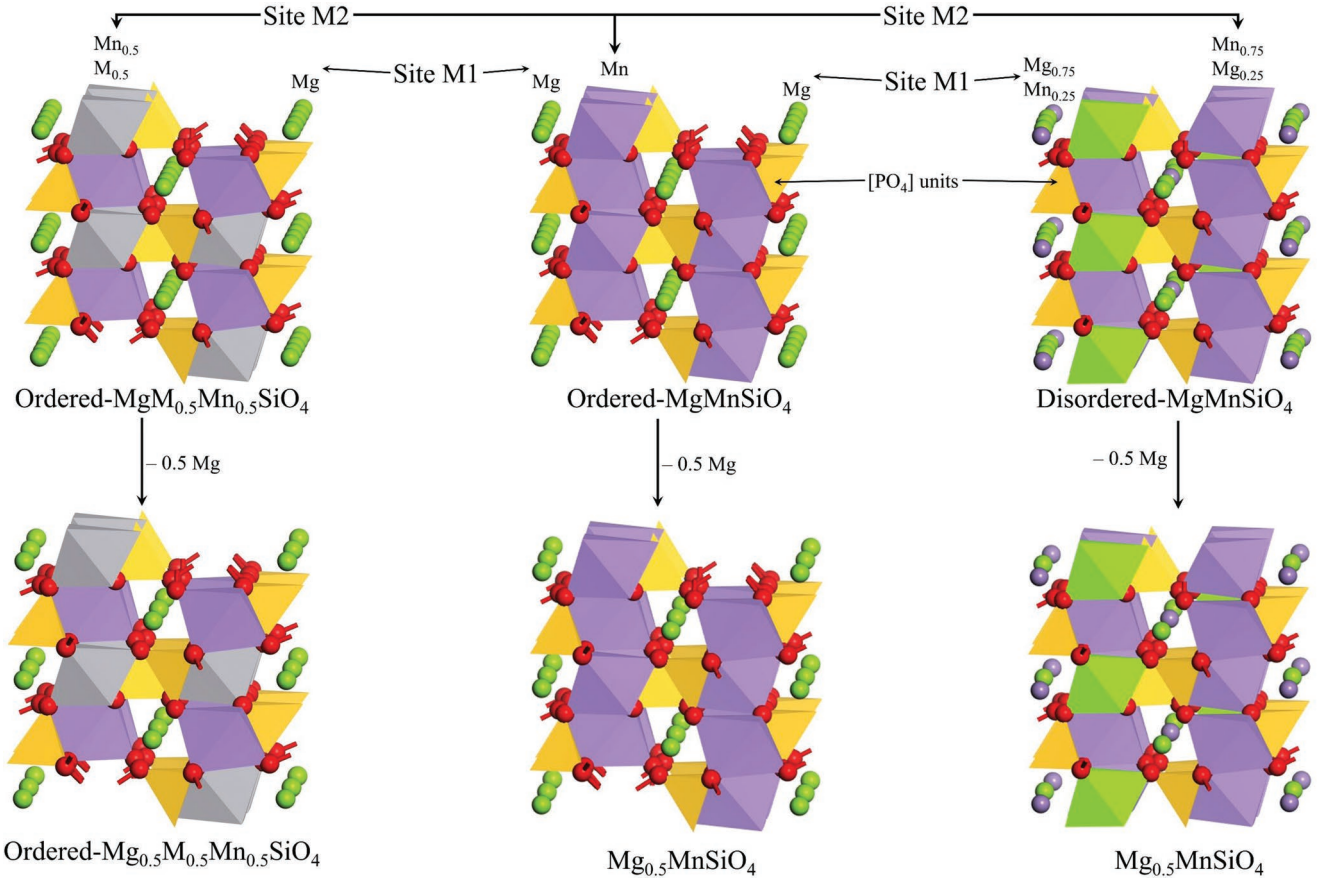

Scheme 1. Top: Structural model for the disordered phase $(Mg_{0.75}Mn_{0.25})_{M1}(Mg_{0.25}Mn_{0.75})_{M2}SiO_4$ (right), ordered phase $(Mg)_{M1}(Mn)_{M2}SiO_4$ (center), and the Mn-substituted $(Mg)_{M1}(M_{0.5}Mn_{0.5})_{M2}SiO_4$ (left). Bottom: same phases after extraction of 0.5 mole of Mg^{2+} from the site M1.

works (**Figure 1**; **Table 1**, reliability factor GoF = 1.55) based on $(Mg_{1-\gamma}Mn_{\gamma})_{M1}(Mg_{\gamma}Mn_{1-\gamma})_{M2}SiO_4$ cations distribution model.[6,7] The Mg/Mn exchange ratio (γ) is ≈0.37 (**Table 2**). The geometry optimization of $(Mg)_{M1}(Mn)_{M2}SiO_4$ (ordered, without cations exchange, that is, $\gamma = 0$) and $(Mg_{0.75}Mn_{0.25})_{M1}(Mg_{0.25}Mn_{0.75})_{M2}SiO_4$ (disordered, with cations exchange of γ = 0.25) is carried out by DFT (Figure 1).[10,11] In both cases the computed unit cell parameters agree well with the experimental refinement results. Without considering entropy, the calculations show that the ordered phase is more stable than the disordered phase from the energy point of view, being the difference of 0.127 eV per unit cell. On increasing the temperature, the entropy term becomes more important, making the disordered phase more stable (Note S1, Supporting Information), as experimentally observed.

The full extraction of Mg from the ordered $(Mg)_{M1}(Mn)_{M2}SiO_4$ phase takes place in two steps, at ≈4.0 and 3.0 V formally involving the multi-electron redox reactions of Mn^{4+}/Mn^{3+} and Mn^{3+}/Mn^{2+} redox pairs, respectively.[12–14] The extraction of Mg from M1 site with a Mg/Mn exchange of γ = 0.25, that is, $(Mg_{0.75}Mn_{0.25})_{M1}(Mg_{0.25}Mn_{0.75})_{M2}SiO_4$ has been also carefully computed. In a first step, 0.50 Mg^{2+} ions are extracted at 2.92 V, formally involving the Mn^{3+}/Mn^{2+} redox pair. The 0.25 Mg^{2+} ions remaining in M1 site are extracted at ≈3.5 V, accompanied by a formal partial oxidation of Mn^{3+} into Mn^{4+}. Due to the exchange of Mg and Mn in sites M1 and M2, the Mg atoms in M2 sites cannot be extracted, thus reducing the total capacity of the compound. Additionally, some Mg atoms could be trapped in M1 site due to the presence of no-mobile Mn atoms in M1 site, thus reducing the total amount of extracted Mg and therefore the extension of the second plateau. In a limit case, only the first plateau could be visible, and thus the expected redox pair involved in the reaction should be Mn^{3+}/Mn^{2+}.

The experimental energy density of 300 W h kg^{-1} has been attained for $MgMnSiO_4$ working within an operating voltage window from 0.5–2.8 V with the principal reaction (160 mA h g^{-1}) occurring at 1.8–2.0 V versus metallic Mg.[7] Lower operational voltage windows have been reported due to the inherent electrolyte instability and corrosion of collectors, thus entailing limited energy density.[15–19]

2.2. Case of Mn Substitution: $MgMn_{0.5}M_{0.5}SiO_4$

We started by substituting half of Mn atoms by Zn. The phase structure and crystallinity of the $MgMn_{0.5}Zn_{0.5}SiO_4$ sample is determined by XRD (Figure 1). The Rietveld refinements confirmed the adequate indexation in the Pnma space group of the orthorhombic system.[6,7] The calculated cell parameters are a = 10.390(3) Å, b = 6.085(2) Å, c = 4.797(1) Å, and V = 303.3 (2) $Å^3$

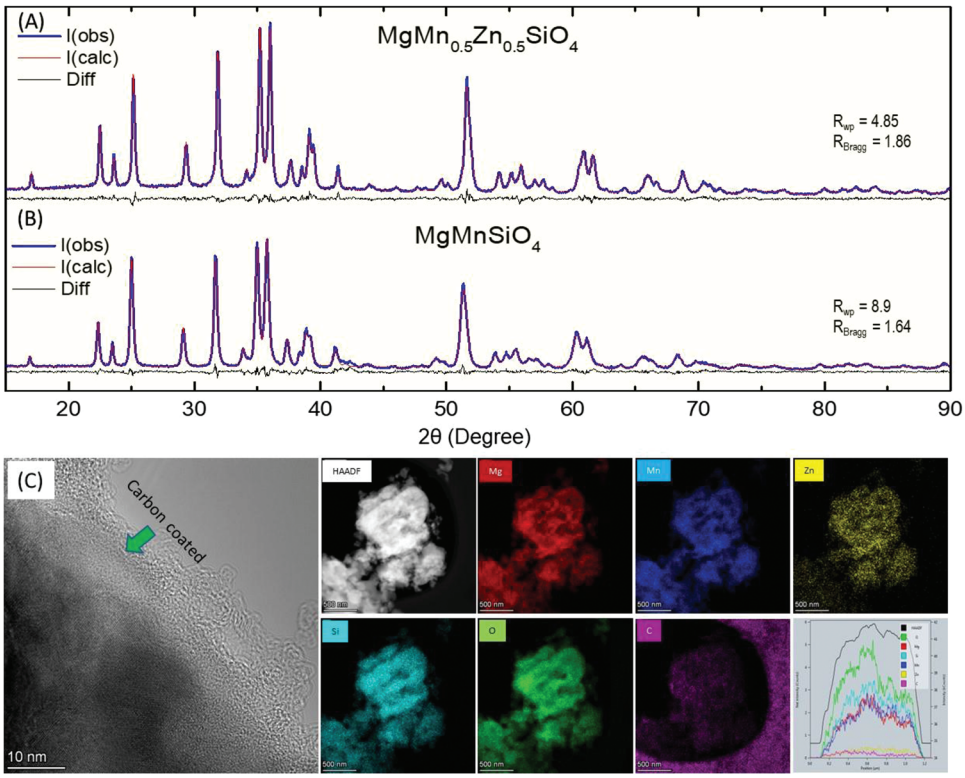

Figure 1. XRD pattern and Rietveld refinement of: A) $MgMn_{0.5}Zn_{0.5}SiO_4$ and B) $MgMnSiO_4$. C) TEM, HAADF-STEM, and EDS elemental mapping of $MgMn_{0.5}Zn_{0.5}SiO_4$.

Table 1. Atomic coordination of $MgMn_{0.5}Zn_{0.5}SiO_4$ and $MgMnSiO_4$ obtained from the Rietveld refinement.

Sample	$MgMnSiO_4$	$MgMn_{0.5}Zn_{0.5}SiO_4$
Space Group	Pnma	
Atomic position and occupancy	—	—
Mg/Mn/Zn in 4a (0, 0, 0)	—	—
(site M1)	Mg = 0.63 (1)	Mg = 0.58 (8)
—	Mn = 0.37 (1)	Mn = 0.19 (7)
—	—	Zn = 0.24 (7)
Mg/Mn/Zn in 4c (*x*, ¼, *z*)	*x* = 0.2788 (3) *z* = 0.9847 (9)	*x* = 0.2789 (6) *z* = 0.987 (2)
(site M2)	Mg = 0.37 (1)	Mg = 0.43 (8)
—	Mn = 0.63 (1)	Mn = 0.31 (7)
—	—	Zn = 0.26 (7)
Si in 4c (*x*, ¼, *z*)	*x* = 0.0972 (5) *z* = 0.4244 (9)	*x* = 0.0945 (5) *z* = 0.4272 (8)
O in 4c (*x*, ¼, *z*)	*x* = 0.0848 (1) *z* = 0.7670 (2)	*x* = 0.093 (1) *z* = 0.756 (2)
O in 4c (*x*, ¼, *z*)	*x* = 0.4348 (1) *z* = 0.2136 (2)	*x* = 0.447 (1) *z* = 0.229 (2)
O in 8d (*x*, *y z*)	*x* = 0.1618 (9) *y* = 0.049 (1) *z* = 0.271 (2)	*x* = 0.1647 (7) *y* = 0.048 (1) *z* = 0.284 (1)

(reliability factor GoF = 1.42). The replacement of half of Mn^{2+} atoms by other divalent element such as Zn^{2+} leads to a pure $MgMn_{0.5}Zn_{0.5}SiO_4$ sample. Obviously, the cells parameters are somewhat smaller than that of $MgMnSiO_4$ as expected from the smaller ionic radius of Zn^{2+} (0.74 Å) in comparison to that of HS-Mn^{2+} (0.83 Å) hexacoordinated.[20] The detailed structural information of $MgMn_{0.5}Zn_{0.5}SiO_4$ is listed in Table 1.

Scheme 1 presents the Mn-substituted $(Mg)_{M1}(M_{0.5}Mn_{0.5})_{M2}SiO_4$ (left) crystal structure with an olivine-type framework and compares with the structural model for the ordered $(Mg)_{M1}(Mn)_{M2}SiO_4$ phase (center), the disordered $(Mg_{0.75}Mn_{0.25})_{M1}(Mg_{0.25}Mn_{0.75})_{M2}SiO_4$ phase (right), as well as after the extraction of 0.5 Mg^{2+} per f.u. from the M1 site (bottom). The particle size and morphology of $MgMn_{0.5}Zn_{0.5}SiO_4$ are observed with transmission electron microscopy (TEM), as shown in Figure 1C and Figure S1, Supporting Information. Most of the particles exhibit irregular shape due to the agglomeration of smaller primary particles with the sizes near 90–150 nm. A close inspection by TEM reveals that carbon is uniformly coated onto the particle surface. In addition, the High-angle annular dark-field scanning transmission electron microscopy (HAADF-STEM) and EDS elemental mapping results demonstrate that Mg, Mn, Zn, Si, O, and C elements are distributed uniformly.

Galvanostatic cycling is employed to determine the coulombic efficiency in our system as similarly employed for Li, Zn, and Mg.[21–23] **Figure 2**A,B shows a representative cycling voltage profile of the Ti‖Mg cell and the applied galvanostatic

Table 2. Experimental and calculated unit cell parameters, cation distribution expressed as "y" in $(Mg_{1-y}Mn_y)_{M1}(Mg_yMn_{1-y})_{M2}$ SiO_4 and relative energy per unit cell of the most stable configuration.

Parameter	y	a [Å]	b [Å]	c [Å]	V [Å]^3	ΔE [eV]
Experimental	0.37 (1)	10.460	6.134	4.817	309.0	—
Calculated	0	10.660	6.162	4.836	317.7	0
	0.25	10.608	6.162	4.852	317.2	+ 0.127

protocol. It can be observed that the cell completed 50 cycles and presented a reasonable average Coulombic efficiency (CE) of 97.3% calculated according to the "method 1" reported by Adams et al.[21] The cell exhibited a slight increase of the overpotential similarly to that of the Pt||Mg cell using $Mg(TFSI)_2$-based solution.[23]

Comparing the possible extraction of 0.5 Mg from $MgMnSiO_4$ (see discussion in Section 2.1) and from $MgMn_{0.5}M_{0.5}SiO_4$, in the first case only the redox pair Mn^{3+}/Mn^{2+} should be involved. But the inclusion of non-electroactive Zn^{2+} and the presence of only 0.5 manganese atoms in the formula, makes the redox pair Mn^{4+}/Mn^{3+} to be also involved, resulting in an increase of the voltage, as shown in Figure 2C. A comparison of the experimental electrochemical (de)intercalation properties between $MgMnSiO_4$ and $MgMn_{0.5}Zn_{0.5}SiO_4$ indicated a capacity loss of 19% and 11% between the first charge and discharge, respectively (Figure 2C). The capacity loss is assigned to two phenomena such as the slow magnesium-ion diffusion in the silicate and the electrolyte decomposition that forms a surface film on the electrode.[15] Zn is not expected to be electroactive, and this fact is reflected in the galvanostatic curves in terms of capacity, but the most outstanding difference resides on the observation of two pseudo-plateaus at about 1.9 and 1.3 V on discharge and 2.4 and 2.8 V on charge for $MgMn_{0.5}Zn_{0.5}SiO_4$. As discussed below, based on the percolation energy (PE) (approximately PE of Zn^{2+} in the site M1 for $MgMn_{0.5}Zn_{0.5}SiO_4$ is 1.78 eV, and PE for Mn^{2+} in the site M1 is 3.59 eV) the relative mobility of the zinc ions (as compared with manganese) facilitates the observation of these plateaus during the Mg extraction/insertion with a formal oxidation/reduction of Mn^{2+} into Mn^{4+} in accordance with the ex situ X-ray photoelectron spectrometer (XPS) and Electron paramagnetic resonance (EPR) measurements. Then, the zinc-free sample with Mn^{2+} in M1 sites could hinder Mg migration and this fact is reflected by a single charge/discharge curve.

Gathering more details of the electrochemical performance of $MgMn_{0.5}Zn_{0.5}SiO_4$ from galvanostatic charge and discharge within the voltage range of 2.9–0.4 V versus Mg^{2+}/Mg (referred as Mg-cell in **Figure 3**A) are essential. During the first charge, two pseudo-plateaus located between 2.2–2.5 and 2.5–2.9 V are observed, extending ≈60 (Δx = 0.2 Mg^{2+}) and 73 mA h g^{-1} (Δx = 0.24 Mg^{2+}), respectively. On discharge, the Mg-cell also exhibits two plateaus between 2.25–1.5 and 1.5–0.5 V recovering the extracted Mg^{2+} ions on the first charge, with the irreversible capacity of 10 mA h g^{-1}. The charge/discharge capacity is 120.4 mA h g^{-1}, entailing 240 W h kg^{-1} with the average working potential of ≈2.0 V. As Zn is not expected to be electroactive, only 0.5 Mg can be extracted, involving the formal oxidation of Mn^{2+} into Mn^{4+}. From a practical point of view, concerning the total amount of extracted Mg in $MgMnSiO_4$ phase, the practical extracted amount of Mg approaches 0.5. In the case of substituting Mn by other electroactive elements (such as Ni and Fe) instead of a non-electroactive one (as Zn), other redox pairs could also be involved (Table S1, Supporting Information), thus varying the voltage of this plateau.

The kinetic response in the first cycle has been studied by adopting various charge/discharge rates ranging from 5 to 60 mA g^{-1} (Figure S2, Supporting Information). With the increase of current density, the galvanostatic curves exhibited a typical diminution in capacity, fluctuation of the charge/discharge cycle efficiency and an increased polarization. The obtained capacities at charge/discharge are 135.1/120.4, 122/111.3, 111.1/105.2, 101.3/96.6, and 90/77.2 mA h g^{-1} for 5, 10, 15, 30, and 60 mA g^{-1}, respectively; and the efficiency at the respective rates resulted in 89%, 91%, 94%, 94.7%, and 85%. These findings are owed to the kinetic hindrance when a fast kinetic is applied to magnesium migration in $MgMn_{0.5}Zn_{0.5}SiO_4$. Moreover, we observed that Zn-doped sample exhibits 78.7% of capacity retention over 45 cycles (Figure S3, Supporting Information) which is higher than that of Zn-free sample (67.4%). Therefore, the comparison of Coulombic efficiency during cycling also confirms that the Zn doping helps to boost the cycling performance irrespectively of a lower initial capacity. These results agree with the report by Liu et al.[24] for doped $LiZn_{0.01}Fe_{0.99}PO_4$. These authors found that Zn^{2+} in the lattice acts as a pillar to prevent the collapse of crystal during cycling. As mentioned above, $MgMn_{0.5}Zn_{0.5}SiO_4$ with only 0.5 manganese atoms per formula could be the reason to activate the Mn(II)/Mn(III)/Mn(IV) redox couple for achieving extraction/insertion of 0.44/0.4 Mg^{2+} ion (0.88/0.8 electrons) according to electrochemical profile (Figures 2C and 3A).

The development of electrode materials for batteries requires fundamental research studies in terms of electrochemical performance. Up to now, several research groups have performed simultaneous investigations of typical materials such as V_2O_5, $Li_4Ti_5O_{12}$, and C in Li-, Na-, Ca-, and/or Mg-ion cells and the related performance provided insightful findings.[25–27] Although such cells are easy to assemble and provide sufficient information, researchers should be concerned of any effects that may influence the electrochemical performance, and their corresponding results should be taken with attention to highlight the observed differences in the battery performance.[28] In the present work, we have found interesting changes in the electrochemical performance of $MgMn_{0.5}Zn_{0.5}SiO_4$ cathode used in Mg- and Na-ion cell configuration. As Na^+ (1.02Å) is ≈30% larger than Mg^{2+} (0.72Å) the latter one moves easier than sodium implying that the effect of ionic radii is important in these systems. For instance, an improved polarization of the Mg-cell (ΔV = 1.25 V) is observed as compared to those cells

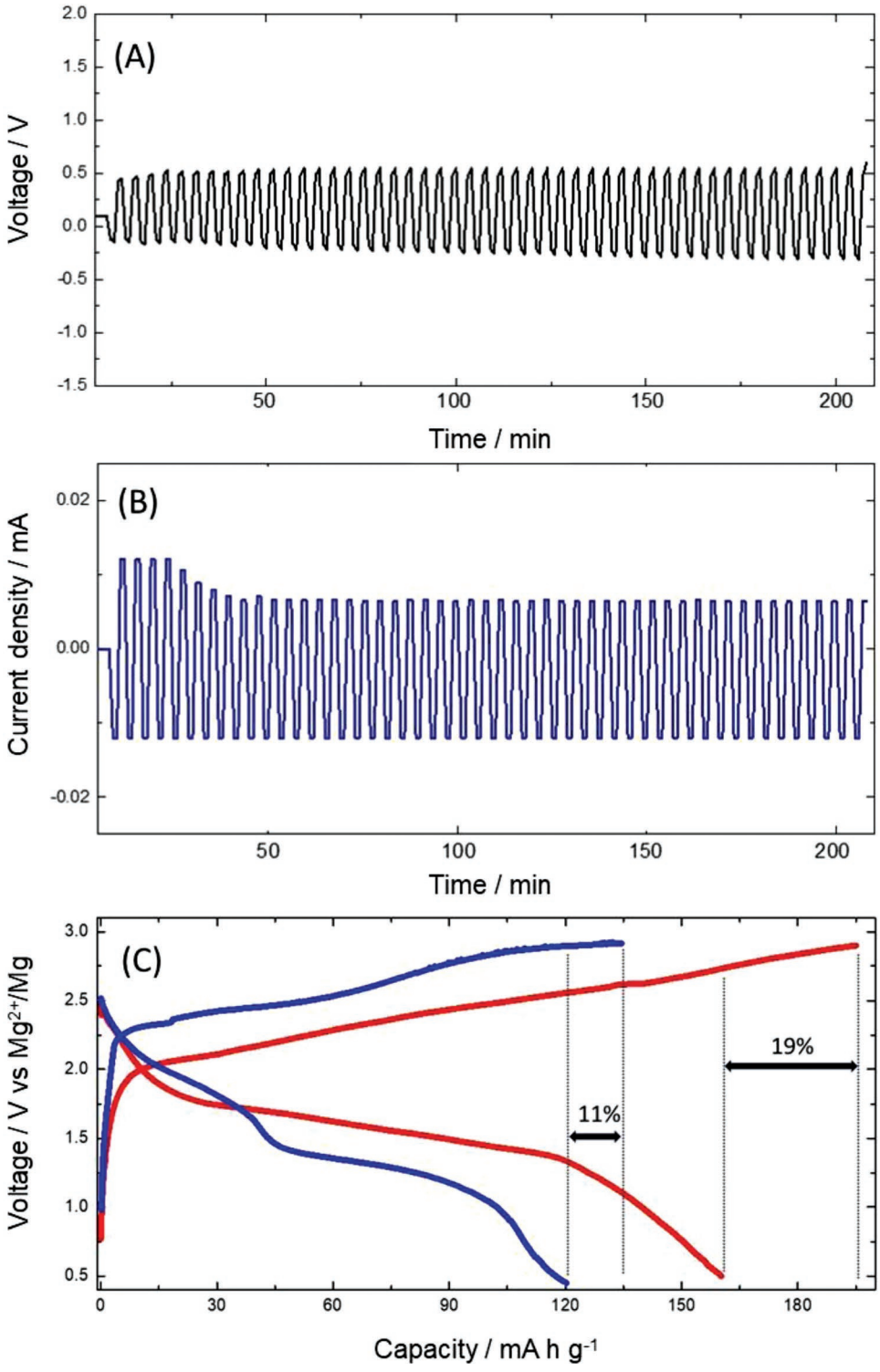

Figure 2. A) The measured voltage versus time plot of Ti‖Mg cell, and B) the employed constant current protocol with 0.008 mA cm^{-2} on discharge and 0.008–0.004 mA cm^{-2} on charge. The areal capacity is about 0.12 mA h cm^{-2}. C) Comparison of the electrochemical Mg (de)intercalation properties between $MgMnSiO_4$ (red color) and $MgMn_{0.5}Zn_{0.5}SiO_4$ (blue color).

with sodium as a counter electrode (Figure 3C,D). These blank experiments have been obtained using two different sodium cells that employ hybrid concepts due to the inherent property of having magnesium in the cathode structure. For one hand the Na/Mg-cell#1 utilized $MgMn_{0.5}Zn_{0.5}SiO_4$ cathode and 1 M $NaClO_4$-PC electrolyte and displayed $\Delta V = 3.9$ polarization. On the other hand, the Na/Mg-cell#2 utilized $MgMn_{0.5}Zn_{0.5}SiO_4$ cathode and a mixture of both 0.5 M $Mg(TFSI)_2$-DME + 1 M

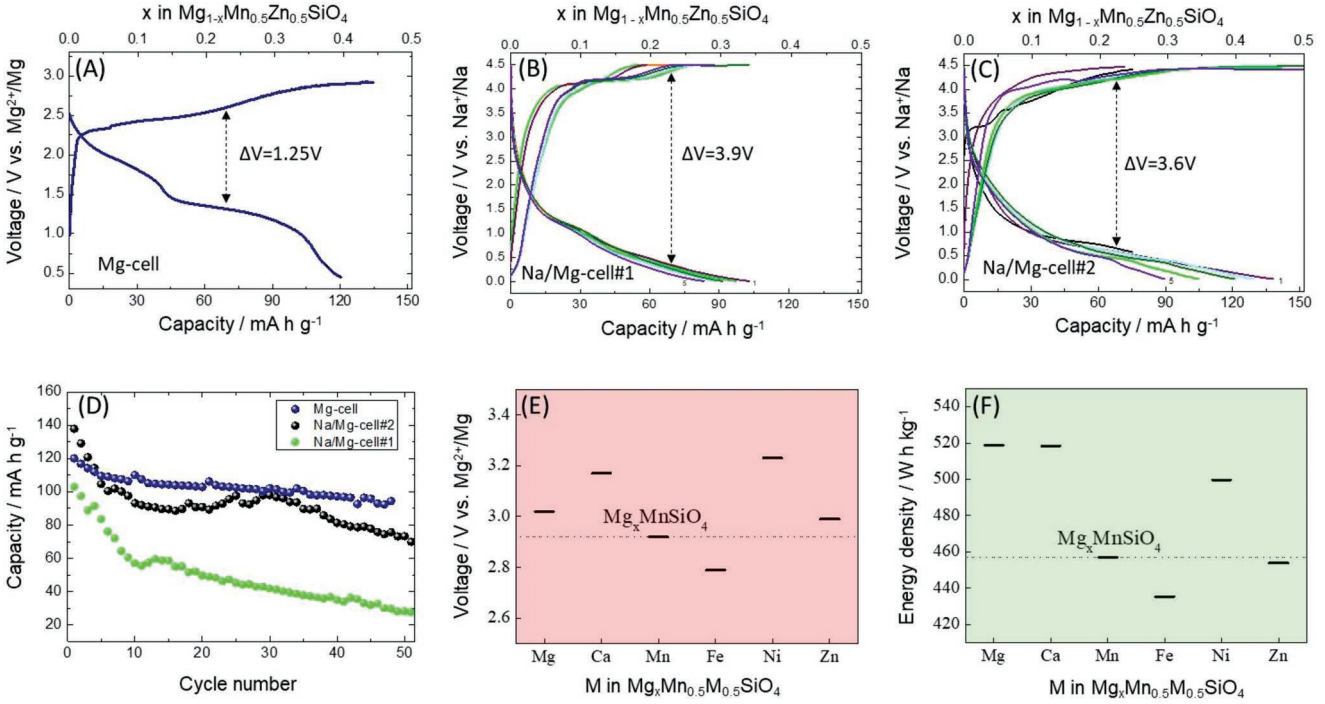

Figure 3. Galvanostatic charge/discharge curve of $MgMn_{0.5}Zn_{0.5}SiO_4$: A) versus metallic Mg (labeled as Mg-cell), B) versus metallic sodium with electrolyte of 1 M $NaClO_4$ in PC:FEC(98:2) (labeled as Na/Mg-cell#1), and C) versus metallic sodium and mixture (1:1 vol.) of 0.5 M $Mg(TFSI)_2$ in DME + 1 M $NaClO_4$ in PC:FEC(98:2) (labeled as Na/Mg-cell#2). D) The capacity retention of the previous cells. E) Calculated averaged voltage and F) energy density corresponding to the extraction of 0.5 Mg per f.u. from $MgMn_{0.5}M_{0.5}SiO_4$ for the different M elements.

$NaClO_4$-PC electrolytes and displayed ΔV = 3.6 polarization. The high polarization and fast capacity fading are normally due to the slow Mg^{2+} ion diffusion and the high polarity of Mg^{2+} specifically when cycling at a high rate.[29–34] The partial replacement of Mn by Zn in the $MgMnSiO_4$ olivine-type structure has a beneficial effect on minimizing the polarization in Mg-cells contrary to what is observed in Na/Mg-cell#1 and #2. According to the results of our Mg and Mg/Na cells, these findings compared favorably with that found in iron-based mixed-polyanion compounds $Li_xNa_{4-x}Fe_3(PO_4)_2(P_2O_7)$ (x = 0–3) in which the redox potential of each phase was ≈3.4 V for the Li-ion cell and ≈3.2 V for the Na-ion cell.[35]

Moreover, the capacity stability is improved in the presence of magnesium in the electrolyte and counter electrode. Its discharge capacity is retained from 120 to 93.5 mA h g^{-1} during 45 cycles (77%). As comparison, the capacity of Na/Mg-cell#1 drops quickly from 102 to 29 mA h g^{-1}, and Na/Mg-cell#2 maintained a relatively more stable capacity retention over 50 cycles from 140 to 75 mA h g^{-1} (53%). Theoretically, 151.8 mA h g^{-1} is assigned to 0.5 de-inserted Mg^{2+} from $MgMn_{0.5}Zn_{0.5}SiO_4$ (reaction #1):

$$MgMn_{0.5}Zn_{0.5}SiO_4 \rightarrow Mg_{0.5}Mn_{0.5}Zn_{0.5}SiO_4 + 0.5Mg^{2+} + 1e^- \quad (1)$$

According to the galvanostatic curves, 0.44 Mg^{2+} ions are extracted in the first charge process, corresponding to 0.88 electrons, which is nearby the oxidation of 0.5 manganese from Mn(II) to Mn(IV) at an average charge voltage of 2.5 V versus metallic Mg. The Inductively coupled plasma (ICP) results confirmed the extraction of 0.43 Mg^{2+} per f.u. corresponding to 130.6 mA h g^{-1} which is related to the reachable specific charge (Table S2, Supporting Information). The Mg^{2+} is inserted after the subsequent discharge as detected by ICP measurements reaching 0.37 Mg^{2+} per f.u. that correspond to ≈112.3 mA h g^{-1} and the inactivity of Zn during charge/discharge can also be supported by elemental analysis. By combining the results of the electrochemical curves with the ICP measurements, the observed capacity could be perfectly attributed to the capacity of the $Mg/MgMn_{0.5}Zn_{0.5}SiO_4$ cell during the charge/discharge cycle.

With the idea of looking for elements increasing the voltage and the energy density, we examined the effect of different M elements on the voltage and energy density in accordance of 0.5 Mg^{2+} per f.u. As shown in Figure 3E and Table S1, Supporting Information, only in the case of M = Fe the calculated voltage (≈2.8 V) is smaller than that of $MgMnSiO_4$ (≈2.9 V), while a higher voltage is obtained for the other studied elements, especially for Ca and Ni, close to 3.2 V. However, the higher atomic weight of Ni penalizes its energy density, as compared with lighter elements. Thus, the higher energy density could be obtained for M = Mg, Ca, close to 520 W h kg^{-1} (Figure 3F), while for M = Ni the energy density is ≈500 W h kg^{-1}. The lowest value is obtained for M = Fe, with ≈440 W h kg^{-1}, attributing to its low voltage.

EPR and XPS experiments are carried out to probe the redox chemistry (**Figure** 4A,B). EPR spectrum of pristine $MgMn_{0.5}Zn_{0.5}SiO_4$ displays the Mn^{2+} signal with linewidth of 15.5 mT and g-factor of 2.00079 ± 0.0003 ascribed to Mn^{2+} in an octahedrally coordinated environment as detected in previous studies.[36,37] Although the magnetic structure of

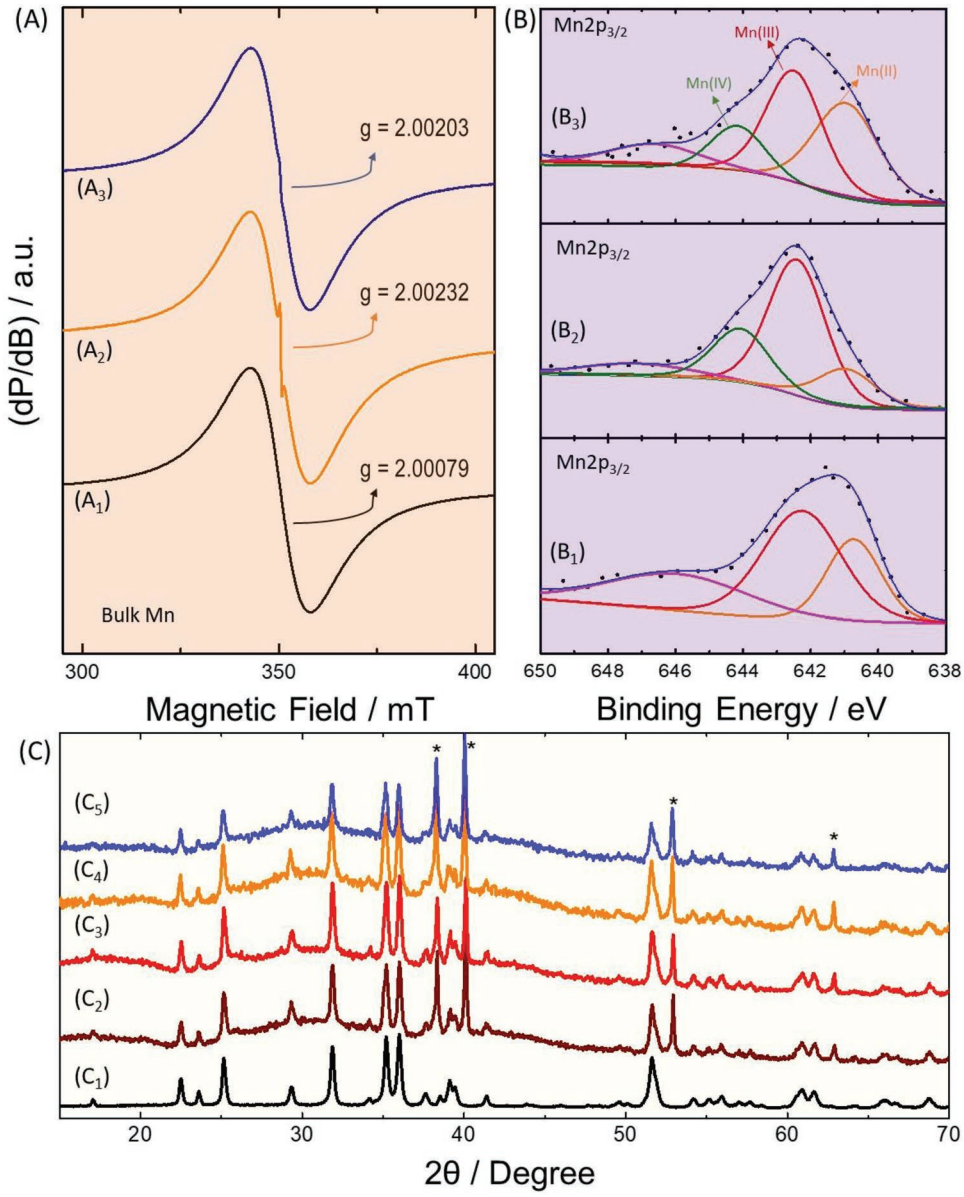

Figure 4. Post-mortem analyses of $MgMn_{0.5}Zn_{0.5}SiO_4$ cathode in Mg-cells. Ex situ EPR spectra of: A_1) pristine, A_2) charged to 2.9 V (extraction of 0.44 Mg^{2+} per f.u.), and A_3) charged to 2.9 V (0.44 Mg^{2+} per f.u.) and subsequent discharged to 0.4 V (0.4 Mg^{2+} per f.u.). Ex situ XPS analysis with detailed fitting of Mn $2p_{3/2}$ core level of: B_1) pristine, B_2) charged to 2.9 V (extraction of 0.44 Mg^{2+} per f.u.), and B_3) charged to 2.9 V (0.44 Mg^{2+} per f.u.) and subsequent discharged to 0.4 V (0.4 Mg^{2+} per f.u.). Ex situ XRD patterns of: C_1) pristine, C_2) 1st charge to 2.9 V (extraction of 0.44 Mg^{2+} per f.u.), C_3) 1st charge/discharge to 0.4. C_4) 6th charge to 2.9 V, and C_5) 14th discharge to 0.4 V. Note that (*) symbol corresponds to the Ti substrate.

$MgMn_{0.5}Zn_{0.5}SiO_4$ is first reported here (Figure 4A), it shows a similar characteristic with Li_2MnSiO_4 and $MgMnSiO_4$ compounds, that is, a main Lorentzian line with $g = 2.003$ at 5 K and $g = 1.99881$ at 293 K,[38] close to the calculated $g = 2.0$ for Mn^{2+} ions in a paramagnetic state.[7] In addition, divalent Zn-ions (with an [Ar] $3d^{10}$ electronic configuration) are EPR silent, therefore the changes of Mn oxidation state from pristine to extracted/inserted $MgMn_{0.5}Zn_{0.5}SiO_4$ at the bulk state in Mg-cell can be monitored by EPR.[39] The extraction of 0.44 mole of Mg^{2+} leads to a transformation of the EPR spectrum resulting in the observation of intensive peak with a g-factor of 2.00232 ± 0.0002 in comparison to that of the original sample. According to the charge curve, the redox couples of Mn^{3+}/Mn^{2+} and Mn^{4+}/Mn^{3+} are responsible for Mg de-insertion. Despite Mn^{3+} ([Ar] $3d^4$) is not measurable by EPR in the X-band region, the signal detected at the end of the total charge is indicative of the co-existence of Mn^{3+} with Mn^{4+}.[7,40–42] The reverse process of the Mg^{2+} insertion leads to a partial restoration of the EPR signal, especially when 0.4 mole of Mg^{2+} is inserted ($g = 2.00203 \pm 0.0004$). This means that charge transformation process during Mg^{2+} intercalation is highly reversible.

The XPS spectra exhibit an asymmetric profile that can be deconvoluted in several components (Figure 4B). The Mn(II) and Mn(III) are detected in the pristine electrode at 640.7 ± 0.3

and 642.3 ± 0.3 eV with the area ratios of 60.2 and 39.8%, respectively;[43] and the presence of Mn(III) in the pristine sample is ascribed to an inevitable oxidation of the particle surface. The satellite peak appeared at ≈646.8 eV (Mn(II)) vanished upon charge.[44] The contribution of Mn(III) and Mn(IV) increased to 68.1 and 21.5% when the electrode is charged to 2.9 V (extraction of 0.44 mole of Mg^{2+} per f.u.) and Mn(II) decreased to 10.4%.[45,46]. After a complete charge (extraction of 0.44 mole of Mg^{2+} per f.u.) followed by discharge (0.4 Mg^{2+} per f.u.), the relative contribution of Mn(II) retrieved the values of the original sample (≈34.5%).

Moreover, to grasp the reaction intercalation mechanism, ex situ XRD patterns are collected after cycling (Figure 4C). The most intense peaks at 22.51°, 23.61°, 25.16°, 29.33°, 31.91°, 35.23°, 35.98°, 39.14°, 41.38°, 51.60°, 54.21°, 55.18°, 60.92°, and 61.66° belong to $MgMn_{0.5}Zn_{0.5}SiO_4$. Those peaks marked with (*) at 38.2°, 39.96°, 52.85°, 62.84°, and 70.55° are assigned to the titanium current collector. The obtained lattice parameters on the first charge are a = 10.359(6) Å, b = 6.064(4) Å, c = 4.790(3) Å, and V = 300.9(3) Å^3, while after the first charge/discharge a = 10.368(6) Å, b = 6.070(4) Å, c = 4.792(3) Å, and V = 301.6(3) Å^3. The calculated volume variation during charging is $\Delta V = -2.4(5)$ Å^3, which is less than 1%. It may not be a significant variation during the discharge/charge process as observed from the lattice planes. The recorded cell parameter after the 6th charge and 14th discharge are a = 10.355(9) Å, b = 6.065(5) Å, c = 4.788(4) Å, V = 300.7(4) Å^3, and a = 10.350(7) Å, b = 6.063(4) Å, c = 4.785(3) Å, and V = 300.3(4) Å^3, respectively, suggesting no significant changes. Thus, the reversible Mg^{2+} (de)insertion (from)into the $MgMn_{0.5}Zn_{0.5}SiO_4$ sample accompanied by the redox activity of the Mn atoms is indirectly inferred by XPS spectra, in agreement with the electrochemical, ICP, EPR, and DFT results.

A comparison of the electronic population before and after Mg extraction derived from Mulliken populations[47] serves to analyze what species (the divalent cations Mg, M and Mn, and the [SiO_4] anion) are involved in the redox process (**Figure 5**A, and Table S3, Supporting Information). In all cases an increase of the positive charge (decrease of the negative charge for oxygen) is observed. Concerning Mn, the calculated charge variation is very similar for all compositions. Also, Mg seems to be involved, with a similar contribution for all compositions excepting M = Zn, with a smaller contribution. Concerning M, the high value of Fe, similar to Mn, suggests that both cations could be involved on the redox process, resulting in a lower oxidation state and thus a lower voltage, as seen above. On the contrary, the contribution of Ca, Ni, and Zn is very small, and these elements seem not to be involved in the redox process. It is also worth noting the important contribution of the [SiO_4] anion, as compared with divalent cations. When represented as a function of the calculated voltage, a general trend is observed as the voltage increases. The lower contribution of M the higher contribution of the [SiO_4] anion is observed, while the contribution of Mg and Mn seems not to be affected by the voltage reaction (Figure 5B).

The calculated values of percolation energy for Mg^{2+} in $Mg_{1-x}Mn_{0.5}Zn_{0.5}SiO_4$ (x = 0, 0.5) is 1.57 ± 0.02 eV, while the percolation energy for Na^+ in $Mg_{0.5}Mn_{0.5}Zn_{0.5}SiO_4$ is 5 ± 0.1 eV, entailing the percolation of Mg^{2+} through "b" axes is favored in comparison to Na^+-ion (**Figure 6**). We think the distribution of electron density surrounding the molecules is inhomogeneous for $MgMn_{0.5}Zn_{0.5}SiO_4$ in Mg-cell as compared to the hybrid concepts. These results can be perfectly in agreement to the observed differences in polarization of ≈5.9 V for Na^+-ion and 1.25 V for Mg^{2+}-ion insertion (Figure 3A–C). To understand the role of Zn, we further calculated the percolation energy of Zn^{2+} in the site M1 for $MgMn_{0.5}Zn_{0.5}SiO_4$. The calculated value, 1.78 eV, is somewhat higher than that of Mg, 1.57 eV, but not so high to hinder Mg^{2+} migration. Thus, the Zn^{2+} mobility can help the Mg extraction. On the contrary, the percolation energy for Mn^{2+} is 3.59 eV, confirming that the Mn atoms in M1 site are not mobile and can hinder Mg diffusion. As the Mn content in M1 site is lower in $MgMn_{0.5}Zn_{0.5}SiO_4$ than in $MgMnSiO_4$, a higher Mg mobility is expected for $MgMn_{0.5}Zn_{0.5}SiO_4$. Overall, we do not think that Zn promotes ionic mobility. Zn mobility/diffusion in solids is sluggish because of the high mass and high charge/radius ratio of Zn^{2+} cation. However, the mobility has been demonstrated in some

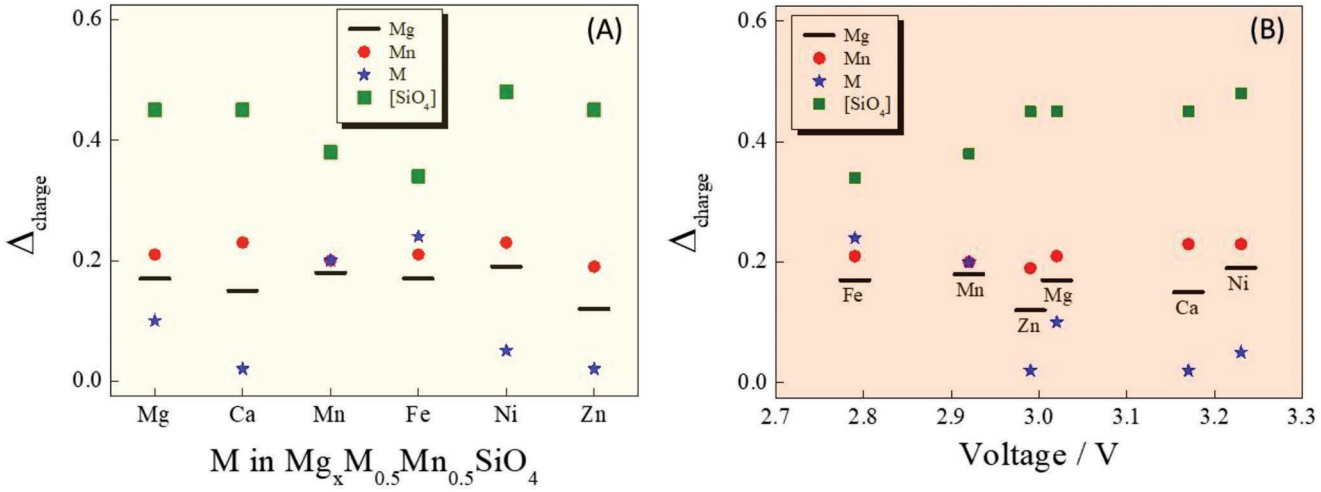

Figure 5. Calculated charge variation for Mg, Mn, M, and [SiO_4] group for the extraction of 0.5 Mg^{2+} per f.u. from $MgM_{0.5}Mn_{0.5}SiO_4$ for: A) the different M elements, and B) as a function of the calculated voltage.

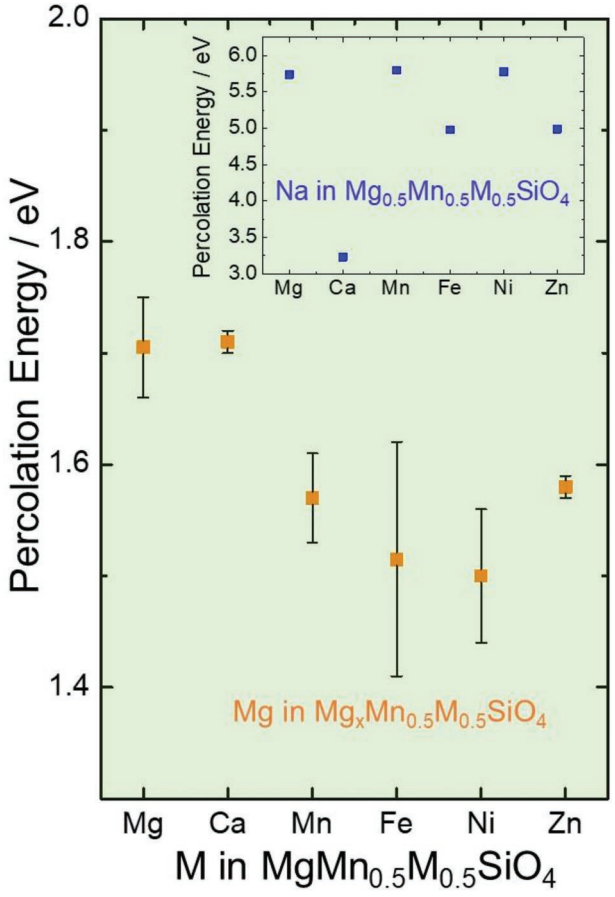

Figure 6. The calculated values of percolation energy for Mg^{2+} in $Mg_{1-x}Mn_{0.5}M_{0.5}SiO_4$ (x = 0, 0.5) and the inset represents the Na^+ in $Mg_{0.5}Mn_{0.5}M_{0.5}SiO_4$.

materials, such as manganese oxides, vanadium oxides, layered sulphides, and Prussian blue analogues. This mobility, although sluggish, is higher than the mobility of Mn cations in the olivine phases studied, as revealed by the percolation energy. Thus, if Mn atoms share the diffusion tunnels with Mg, then Mn can block Mg diffusion. But if some Mn atoms are substituted by Zn, then this sluggish mobility of Zn could help the Mg diffusion, at least more than Mn can help. However, the side effect of the presence of Zn (replacing Mn) could be a diminished electronic conductivity. Both ionic and electronic conductivity could be responsible of the overall voltage hysteresis.[24,48]

Eventually, we extended the calculation of the percolation energy to the other M elements studied (Mg, Ca, Fe, Ni), to examine the potential application of these olivine-type composition for high power batteries, using the BVEL approach and softBV parameters. The calculated Mg^{2+} percolation energy is near the range 1.5 to 1.7 eV (Figure 6). For the sake of comparison, we have also calculated the percolation energy of Li^+ in the system $FePO_4/LiFePO_4$ which varies in the range 0.3 to 0.7 eV. According to these results, we conclude that olivine-type $Mg_{1-x}Mn_{0.5}M_{0.5}SiO_4$ materials are promising for high energy and low power Mg^{2+}-based batteries and applications.[49,50]

3. Conclusions

In summary, to the best of our knowledge, olivine-type $MgMn_{0.5}Zn_{0.5}SiO_4$ material is reported here first, as well as its atomic coordinates and crystal structure revealed by XRD and Rietveld refinement, ICP, EPR, and XPS. This Zn-substituted phase is used as cathode material for Mg-batteries for first time using metallic Mg as anode. And it has not been used in the field of lithium and sodium ion batteries either. Additionally, the structural models for the disordered $(Mg_{0.75}Mn_{0.25})_{M1}(Mg_{0.25}Mn_{0.75})_{M2}SiO_4$ phase and ordered $(Mg)_{M1}(Mn)_{M2}SiO_4$ phase are reasonably explained before and after magnesium (de)-insertion. Zn is a cheap and inactive element in terms of electrochemical responses in $MgMn_{0.5}Zn_{0.5}SiO_4$, but could decrease the capacity loss and improve the Coulombic efficiency. Our recent experience demonstrates that Zn is a reliable strategy to improve the structural stability of layered sodium oxides for sodium-ion batteries. For example, serving as "pillars" to alleviate the structure destruction during repeated electrochemical cycling.[51,52] In this olivine-type structure, Zn remains in M2 and M1 sites and helps to boost the cycling performance as compared to $MgMnSiO_4$. Moreover, the experimental and theoretical calculation results demonstrate that partial replacement of Mn^{2+} in Oh sites by other divalent metal such as Zn^{2+} lowers the cell polarization in comparison to Na-cell counterparts, since the main instabilities caused in Mn-tetrahedral such as in Li_2MnSiO_4 are avoided. Furthermore, this work foresees to extend the study to other divalent elements in olivine-type $(Mg)_{M1}(Mn_{0.5}M_{0.5})_{M2}SiO_4$ structure with M = Ni^{2+}, Ca^{2+}, Fe^{2+}, and Mg^{2+} which has effective impact on the voltage and the energy density as revealed by DFT calculations. According to the calculated Mg^{2+} percolation energy we conclude that olivine-type $Mg_{1-x}Mn_{0.5}M_{0.5}SiO_4$ materials are particularly attractive for low power Mg^{2+}-based batteries. Therefore, these results may open new approaches to design suitable cathodes for next generations' Mg-batteries.

4. Experimental Section

Materials Preparation: The $MgMn_{0.5}Zn_{0.5}SiO_4$ sample was prepared by a sol–gel process. The starting reagents, supplied by Merk-Sigma-Aldrich were magnesium (II) acetate tetrahydrate ($Mg(CH_3COO)_2{\cdot}4H_2O$), manganese(II) acetate tetrahydrate ($Mn(CH_3COO)_2{\cdot}4H_2O$), zinc (II) acetate tetrahydrate $Zn(CH_3COO)_2{\cdot}4H_2O$, and tetraethoxysilane ($C_8H_{20}O_4Si$). For instance, 0.02575 mol $Mg(CH_3COO)_2{\cdot}4H_2O$ are dissolved into 60 mL of ethanol and magnetically stirred for 15 min. Next, 0.01213 mol of $Mn(CH_3COO)_2{\cdot}4H_2O$ and 0.01213 mol of $Zn(CH_3COO)_2{\cdot}4H_2O$ were added and stirred for 30 min. Then, 0.02575 mol of tetraethoxysilane was poured into the previous solution and kept thoroughly stirring for 1 h. The mixture was stirred at 60 °C under reflux for 24 h to form a white suspension, which was then dried at 80 °C under vacuum for 24 h. To get an ≈5% of carbon coating around the silicate samples, 0.54 g of sucrose and 3.64 g of the Mg—Mn—M—Si—O precursor were ball-milled at 350 rpm for 20 h in acetone. After drying and thoroughly milling by hand, the obtained powder was pelletized and heated at 900 °C for 24 h under argon atmosphere. The model $MgMnSiO_4$ sample was prepared using the similar procedure but without adding zinc to the solution.

Characterization: XRD patterns were recorded on a BrukerD8 Discover A25 diffractometer with Cu Kα radiation and Ge monochromator (λ = 1.5406 Å) and LYNXEYE detector at the scan rate of a 0.5°/min between

15° and 90°. The TEM images and HAADF-STEM were performed at 200 kV on a FEI Talos F200 microscope. To analyze the chemical state of the elements, an XPS (SPECS Phoibos 150 MCD) equipped with a monochromatic Al Kα source was used. The C 1s line of the carbon (284.6 eV) was used as the reference. EPR spectra were recorded in a Bruker EMX instrument operating at X-band and 9.75 GHz. Inductively coupled plasma mass spectrometry (ICP-MS) was performed with NexION 350X from PerkinElmer (Waltham, MA, USA) apparatus. A microwave system UltraWave by Milestone (Shelton, USA) was used for the digestion of the samples using a mixture of nitric and hydrofluoric acid (Suprapur de Merck).

Calculations: DFT calculations were carried out in the generalized-gradient approximation (GGA) as implemented in the CASTEP code.[10] The PBEsol correlation potential and a density-mixing scheme with a conjugate-gradient Pulay solver were used. The selected k-point mesh was of ≈0.07 Å^{-1}, following to the Monkhorts–Pack scheme. The cut-off energy was fixed at 600 eV. Spin polarized calculations were performed in all cases. Unit cell parameters and atomic coordinates were relaxed. The internal coordinates were optimized using the BFGS algorithm. The convergence conditions used were: energy, 10^{-5} eV per atom; max. force, 0.03 eV Å^{-1}; max. stress, 0.05 GPa and max. displacement, 10^{-3} Å. For the GGA + U correction the value U_f = 3.9 was used for the d-state of Mn, 5.3 V for Fe and 6.2 for Ni.[11] The percolation energy was calculated using BVEL approach, as implemented in the software BondStr software included in the FullProf Suite package. In calculations, soft bond valence parameters (softBV) were used. The structural parameters and atomic coordinates used in BVEL were those optimized by DFT.

Electrochemical Measurements: The electrodes were prepared by painting an 80:10:10 weight ratio mixture of $MgMn_{0.5}Zn_{0.5}SiO_4$, carbon black, and polyvinylidene fluoride (PVDF) binder on Ti foils (99% purity and 0.127 mm thickness) followed by drying at 120 °C for 5 h. The anode was a metallic Mg ribbon (Aldrich, 99.5% purity). It was cleaned with H_2O:HCl (ratio 40:1% vol.) and then dried at 80 °C. The cells were assembled in the glove box and galvanostatic charge–discharge tests were conducted on the LAND CT-2001A (Wuhan, China) and biologic VMP battery test systems. The electrolyte was 0.5 M $Mg(TFSI)_2$ (with 16% of water content) in DME (dimethoxymethane) as electrolyte as previously reported.[13,14] The cells were tested under controlled temperature between 25–27 °C. The Mg-cells and Na-cells were recorded at 5 mA g^{-1}.

Ti‖Mg cells were employed to quantify the Coulombic efficiency (CE) of the electrolyte and the overpotential caused by metallic Mg anode using constant current protocol with 0.008 mA cm^{-2} on discharge and 0.008–0.004 mA cm^{-2} on charge. Both foils were polished using sandpaper. For the Mg deposition on the Ti foil (1.54 cm^2 active surface area) and calculation of CE, the method 1 described by Adams et al.[21] was used. A Neware battery testing station and a temperature control chamber set at 30 °C were used for such experiments.

Supporting Information

Supporting Information is available from the Wiley Online Library or from the author.

Acknowledgements

This work was financially supported by the "Junta de Andalucía" (Proyecto de Excelencia: 0001020, UCO-FEDER: 1380025-R and FQM288). The authors thank the support research service from SCAI (ICP and XPS) and IQUEMA at the University of Córdoba. Also, this work was financially supported by the National Key Research and Development Program of China (2018YFB0905400 and 709 2016YFB0901502) and the National Natural Science Foundation of China (21761132030, 21621091, 21428303, and 711 21233004). Dr. W. Zuo acknowledges the scholarship from the Alexander von Humboldt Foundation. Prof. Ortiz acknowledges the financial support from the Xiamen University Foreign Young Talents Program (G2022149004L).

Conflict of Interest

The authors declare no conflict of interest.

Data Availability Statement

The data that support the findings of this study are available from the corresponding author upon reasonable request.

Keywords

batteries, density functional theory (DFT), magnesium, $MgMn_{0.5}Zn_{0.5}SiO_4$, olivine, silicate

Received: September 29, 2022
Revised: December 18, 2022
Published online: January 12, 2023

[1] A. K. Padhi, K. S. Nanjundaswamy, J. B. Goodenough, *J. Electrochem. Soc.* **1997**, *144*, 1188.
[2] Y. Gao, Z. Pan, J. Sun, Z. Liu, J. Wang, *Nano-Micro Lett.* **2022**, *4*, 94.
[3] M. J. Park, A. H. Yaghoobnejad, A. Manthiram, *ACS Energy Lett.* **2020**, *5*, 2367.
[4] M. E. Arroyo-de Dompablo, M. Armand, J. M. Tarascon, U. Amador, *Electrochem. Commun.* **2006**, *8*, 1292.
[5] R. Dominko, M. Bele, M. Gaberšček, A. Meden, M. Remškar, J. Jamnik, *Electrochem. Commun.* **2006**, *8*, 217.
[6] A. Torres, M. E. Arroyo-de Dompablo, *J. Phys. Chem. C* **2018**, *122*, 9356.
[7] S. Rubio, Z. Liang, Y. Li, W. Zuo, P. Lavela, J. L. Tirado, R. Liu, K. Zhou, J. Zhu, B. Zheng, X. Liu, Y. Yang, G. F. Ortiz, *Electrochim. Acta* **2022**, *404*, 139738.
[8] C. A. Francis, P. H. Ribbe, *Am. Mineral.* **1980**, *65*, 1263.
[9] S. A. T. Redfern, *Phys. B* **1998**, *241–243*, 1189.
[10] S. J. Clark, M. D. Segall, C. J. Pickard, P. J. Hasnip, M. J. Probert, K. Refson, M. C. Payne, *Z. Kristallogr. Cryst. Mater.* **2005**, *220*, 567.
[11] A. Jain, S. P. Ong, G. Hautier, W. Chen, W. D. Richards, S. Dacek, S. Cholia, D. Gunter, D. Skinner, G. Ceder, K. A. Persson, *APL Mater.* **2013**, *1*, 011002.
[12] C. Ling, D. Banerjee, W. Song, M. Zhang, M. Matsui, *J. Mater. Chem.* **2012**, *22*, 13517.
[13] R. Ruiz, C. Pérez-Vicente, S. Rubio, R. Stoyanova, W. Zuo, Y. Yang, G. F. Ortiz, *Energy Storage Mater.* **2022**, *48*, 12.
[14] S. Rubio, R. Liu, X. Liu, P. Lavela, J. L. Tirado, Q. Li, Z. Liang, G. F. Ortiz, Y. Yang, *J. Mater. Chem. A* **2019**, *7*, 18081.
[15] Z. Feng, J. Yang, Y. NuLi, J. Wang, *J. Power Sources* **2008**, *184*, 604.
[16] Y. NuLi, J. Yang, J. Wang, Y. Li, *J. Phys. Chem. C* **2009**, *113*, 12594.
[17] Y. NuLi, J. Yang, Y. Li, J. Wang, *Chem. Commun.* **2010**, *46*, 3794.
[18] Z. Feng, J. Yang, Y. NuLi, J. Wang, X. Wang, Z. Wang, *Electrochem. Commun.* **2008**, *10*, 291.
[19] Y. Li, Y. Nuli, J. Yang, T. Yilinuer, J. Wang, *Chin. Sci. Bull.* **2011**, *56*, 386.
[20] R. D. Shannon, *Acta Crystallogr.* **1976**, *A32*, 751.
[21] B. D. Adams, J. Zheng, X. Ren, W. Xu, J. G. Zhang, *Adv. Energy Mater.* **2018**, *8*, 1702097.
[22] L. Ma, M. A. Schroeder, O. Borodin, T. P. Pollard, M. S. Ding, C. Wang, K. Xu, *Nat. Energy* **2020**, *5*, 743.

[23] R. Attias, B. Dlugatch, O. Blumen, K. Shwartsman, M. Salama, N. Shpigel, D. Sharon, *ACS Appl. Mater. Interfaces* **2022**, *14*, 30952.
[24] H. Liu, Q. Cao, L. J. Fu, C. Li, Y. P. Wu, H. Q. Wu, *Electrochem. Commun.* **2006**, *8*, 1553.
[25] G. G. Amatucci, F. Badway, A. Singhal, B. Beaudoin, G. Skandan, T. Bowmer, I. Plitz, N. Pereira, T. Chapman, R. Jaworski, *J. Electrochem. Soc.* **2001**, *148*, A940.
[26] G. Hasegawa, K. Kanamori, T. Kiyomura, H. Kurata, K. Nakanishi, T. Abe, *Adv. Energy Mater.* **2015**, *5*, 1400730.
[27] S. Rubio, R. Ruiz, W. Zuo, Y. Li, Z. Liang, D. Cosano, J. Gao, Y. Yang, G. F. Ortiz, *ACS Appl. Mater. Interfaces* **2022**, *14*, 43127.
[28] J. Muldoon, C. B. Bucur, T. Gregory, *Chem. Rev.* **2014**, *114*, 11683.
[29] Y. Wang, R. Chen, T. Chen, H. Lv, G. Zhu, L. Ma, C. Wang, Z. Jin, J. Liu, *Energy Storage Mater.* **2016**, *4*, 103.
[30] S. Rubio, Z. Liang, X. Liu, P. Lavela, J. L. Tirado, R. Stoyanova, E. Zhecheva, R. Liu, W. Zuo, Y. Yang, C. Pérez-Vicente, G. F. Ortiz, *Energy Storage Mater.* **2021**, *38*, 462.
[31] X. Lei, X. Liang, R. Yang, F. Zhang, C. Wang, C. S. Lee, Y. Tang, *Small* **2022**, *18*, 2200418.
[32] Y. NuLi, Y. Zheng, J. Chen, F. Wang, J. Yang, A. I. Minett, J. Wang, *Electrochem. Commun.* **2011**, *13*, 1143.
[33] J. Eaves-Rathert, K. Moyer, M. Zohair, C. L. Pint, *Joule* **2020**, *4*, 1324.
[34] H. D. Yoo, I. Shterenberg, Y. Gofer, G. Gershinsky, N. Pour, D. Aurbach, *Energy Environ. Sci.* **2013**, *6*, 2265.
[35] H. Kim, I. Park, D. H. Seo, S. Lee, S. W. Kim, W. J. Kwon, Y. U. Park, C. S. Kim, S. Jeon, K. Kang, *J. Am. Chem. Soc.* **2012**, *134*, 10369.
[36] N. Abhyankar, Y. E. Ghoussoub, Q. Wang, N. S. Dalal, J. B. Schlenof, *J. Phys. Chem. B* **2016**, *120*, 6771.
[37] E. N. Zhecheva, M. Y. Gorova, R. K. Stoyanova, *J. Mater. Chem.* **1999**, *9*, 1559.
[38] I. Belharouak, A. Abouimrane, K. Amine, *J. Phys. Chem. C* **2009**, *113*, 20733.
[39] R. Stoyanova, E. Zhecheva, S. Vassilev, *J. Solid State Chem.* **2006**, *179*, 378.
[40] T. Boyadzhieva, V. Koleva, E. Zhecheva, D. Nihtianova, L. Mihaylov, R. Toyanova, *RSC Adv.* **2015**, *5*, 87694.
[41] R. Stoyanova, D. Carlier, M. Sendova-Vassileva, M. Yoncheva, E. Zhecheva, D. Nihtianova, C. Delmas, *J. Solid State Chem.* **2010**, *183*, 1372.
[42] M. Yoncheva, R. Stoyanova, E. Zhecheva, E. Kuzmanova, M. Vassileva Sendova, D. Nihtianova, D. Carlier, M. Guignard, C. Delmas, *J. Mater. Chem.* **2012**, *22*, 23418.
[43] U. Nisar, R. A. Shakoor, R. Essehli, R. Amin, B. Orayech, Z. Ahmad, P. R. Kumar, R. Kahraman, S. Al-Qaradawi, A. Soliman, *Electrochim. Acta* **2018**, *292*, 98.
[44] M. C. Biesinger, B. P. Payne, A. P. Grosvenor, L. W. M. Lau, A. R. Gerson, Smart, R. S. C. Smart, *Appl. Surf. Sci.* **2011**, *7*, 2717.
[45] T. Mori, T. Masese, Y. Orikasa, Z. D. Huang, T. Okado, J. Kim, Y. Uchimoto, *Phys. Chem. Chem. Phys.* **2016**, *18*, 13524.
[46] Q. D. Truong, M. K. Devaraju, I. Honma, *J. Power Sources* **2017**, *361*, 195.
[47] R. Mulliken, *J. Chem. Phys.* **1995**, *23*, 1833.
[48] S. Y. Chung, J. T. Bloking, Y. M. Chiang, *Nat. Mater.* **2002**, *1*, 123.
[49] M. Song, Y. Wang, B. Yu, W. Yang, G. Cheng, W. Cui, Z. Zhang, *Chem. Eng. J.* **2022**, *450*, 138176.
[50] C. Wang, Y. Huang, Y. Lu, H. Pan, B. B. Xu, W. Sun, M. Yan, Y. Jiang, *Nano-Micro Lett.* **2021**, *13*, 195.
[51] W. Zuo, J. Qiu, C. Hong, X. Liu, J. Li, G. F. Ortiz, Q. Li, S. Zheng, G. R. Zheng, Y. Yang, *ACS Appl. Energy Mater.* **2019**, *2*, 4914.
[52] W. Zuo, J. Qiu, X. Liu, B. Zheng, Y. Zhao, J. Li, H. He, K. Zhou, Z. Xiao, Q. Li, G. F. Ortiz, Y. Yang, *Energy Storage Mater.* **2020**, *26*, 503.